PHYSICAL REVIEW B **87**, 020508(R) (2013)

Resistance in transition-edge sensors: A comparison of the resistively shunted junction and two-fluid models

Douglas A. Bennett,* Daniel S. Swetz,† Daniel R. Schmidt,† and Joel N. Ullom
National Institute of Standards and Technology, Boulder, Colorado 80305, USA
(Received 9 October 2012; published 25 January 2013)

The transition between the superconducting and normal states is of extreme practical importance because the very sharp onset of resistance in voltage biased thin films is the basis for transition-edge sensors (TESs). TESs are being successfully utilized in many new instruments despite the fact that there is no consensus model that describes the resistance as a function of both temperature and current $R(T,I)$. A new model assuming a TES can be described as a resistively shunted junction (RSJ) has generated much interest. Here we compare the predictions of this model with the predictions of a two-fluid model and measured data. Except for some small TESs (characteristic size $<125\ \mu$m), the data are not consistent with the RSJ model but are consistent with the two-fluid model.

DOI: 10.1103/PhysRevB.87.020508 PACS number(s): 85.25.Oj, 74.45.+c, 74.20.De, 74.50.+r

A superconducting film electrically biased on the transition between the superconducting and normal states can be utilized as an extremely sensitive thermometer known as a transition-edge sensor (TES). Microbolometers based on TESs have become an indispensable tool for submillimeter and millimeter-wave astronomy instruments due to their high sensitivity, e.g., achieving microkelvin sensitivity in maps of the cosmic microwave background (CMB).[1] This sensitivity has led to a demonstration of gravitational lensing of the CMB,[2,3] an independent confirmation of the existence of dark energy using only the CMB,[4] constraints on the dark energy equation of state,[5] and strong evidence for motions of galaxy clusters and groups via CMB temperature distortions due to the kinematic Sunyaev-Zel'dovich effect.[6] Microcalorimeters based on TESs offer a unique combination of efficiency and energy resolution that is being exploited in a wide range of applications,[7] including studies of the atomic structure of high-Z ions,[8] x-ray materials analysis,[9] gamma-ray spectroscopy for nuclear materials accounting in nonproliferation scenarios,[10] and the search for weakly interacting massive particles (WIMPs).[11] Taking only the last example, the Cryogenic Dark Matter Search experiment has placed the strongest constraints on the WIMP-nucleon spin-independent scattering cross section for a wide range of WIMP masses and excluded new parameter space in inelastic dark matter models. TESs have been extremely successful despite the fact that there is no consensus on the underlying mechanism for the observed finite width of the transition. A physical model that explains the resistance of TESs as a function of both temperature and current $[R(T,I)]$ has been elusive.

Measurements by Sadleir *et al.*[12] of the superconducting critical current (I_c) in TESs from 8 to 290 μm long showed an exponential dependence on the length (L) of the TES. They also observed a Fraunhofer-like pattern for I_c as a function of applied magnetic field. A theory based on the long-range lateral proximity effect was used to describe this behavior as a superconducting weak link between the leads of the TES, where the transition temperature of the superconducting electrodes (T_{cL}) is much larger than the transition temperature of the TES film (T_c). Figure 1(a) shows a photograph (left) and a schematic representation (right) of a typical TES where, in this case, the TES film is a MoCu bilayer suspended on top of a silicon nitride membrane. A superconducting weak link[13] is a weak electrical contact of direct (non-tunnel-type) conductivity between superconducting electrodes. Due to the proximity effect, the order parameter (ψ) of the superconducting electrodes extends into the weak link, decaying exponentially over a distance of the coherence length (ξ). If $\xi \lesssim L$, then the order parameter does not go to zero and supercurrent can traverse the weak link [see Fig. 1(b)]. When $T < T_c$, the TES bilayer thin film is in the superconducting state (S′) and the coherence length is $\xi_{S'}$. When $T > T_c$, the TES bilayer thin film is in the normal state (N′) and the coherence length is $\xi_{N'}$. Except when $L \gg \xi$, the critical current of a weak link depends on L.

The observation of weak-link behavior for the I_c in TESs suggested to Kozorezov *et al.*[14] that a resistively shunted junction model (RSJ) would contain the essential physics necessary to describe the resistance of a TES. Until the RSJ model is compared to data, it remains an outstanding question whether the weak-link behavior observed at the onset of resistance in some TESs extends into the transition and has an important effect on the $R(I,T)$ surface. In contrast, Irwin *et al.*[15] base their two-fluid model for the resistance of a TES on physics that occurs in the superconducting film rather than originating in the coupling between the leads. This model separates the supercurrent, which is some fraction (c_I) of the critical current, and a quasiparticle current, which is equal to the voltage (V) applied across the TES divided by some fraction (c_R) of the normal resistance. The most promising physical mechanism for the resistance of this form is the model for phase-slip lines (PSLs) proposed by Skocpol-Beasley-Tinkham (SBT).[16] With PSLs as the physical basis for resistance, the SBT model assumes a constant ratio of the time-averaged supercurrent to the bulk critical current, $\overline{I_c}/I_c$. For this model the two-fluid parameters are $c_I = \overline{I_c}/I_c$ and $c_R = 2N\rho_\lambda \Lambda_{Q^*}/R_n$, where ρ_λ is the normal resistance per unit length, Λ_{Q^*} is the charge imbalance relaxation length, and N is the number of phase-slip lines. In this Rapid Communication, the RSJ model will be compared to the two-fluid model[17] and to measured data.

The RSJ model has been used with some success in modeling superconducting weak links.[13] The simplest version

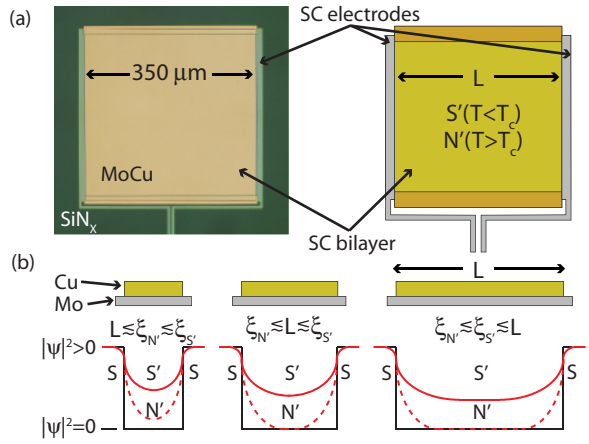

FIG. 1. (Color online) (a) A photograph (left) and diagram (right) of a 350 μm MoCu TES with Mo electrodes. (b) Schematic representation of the modulus squared of the superconducting order parameter for SS′S ($T < T_c$, solid red line) and SN′S ($T > T_c$, dashed red line) in three different length TESs.

of the RSJ model assumes that the resistance is determined by the interaction of the superconducting leads with the TES film in between, rather than any resistive mechanism of the film itself, e.g., nonequilibrium effects, Andreev reflections, phase-slip mechanisms, and conversion from supercurrent to normal current in intervening normal-metal structures. Kozorezov *et al.* base their RSJ model for TESs on a model developed by Coffey *et al.*[18] that describes quantum corrections to the standard Brownian motion of a particle in a tilted washboard potential in the presence of thermal fluctuations. In the classical limit, the resistance of the weak link is

$$R(T,I) = R_n\left(1 + \frac{1}{x}\,\mathrm{Im}\left[\frac{I_{1+i\gamma x}(\gamma)}{I_{i\gamma x}(\gamma)}\right]\right), \tag{1}$$

where R_n is the normal resistance, $x = I/[I_c(T)]$, $I_c(T)$ is the critical current, and $\gamma = [\hbar I_c(T)]/(2ek_BT)$ is the ratio of Josephson coupling energy to thermal energy. $I_{1+i\gamma x}(\gamma)$ and $I_{i\gamma x}(\gamma)$ are modified Bessel functions $I_\nu(z)$ of complex order ν and real variable z. For typical TESs γ is large near the maximum I_c, e.g., $\gamma \approx 10^5$ at $I_c = 1$ mA and $T = 100$ mK, and goes to zero as I_c goes to zero.

When modeling the performance of TESs,[7] the local resistance is parametrized by use of the logarithmic derivatives of resistance with respect to temperature at constant current, $\alpha_I = (T/R)\,(\partial R/\partial T)|_I$, and with respect to current at constant temperature, $\beta_I = (I/R)\,(\partial R/\partial I)|_T$. We therefore compare predictions of α_I and β_I in the two models. Within the RSJ model, α_I and β_I are[14]

$$\alpha_I = -\frac{\gamma}{x}\frac{\partial \ln I_c}{\partial \ln T}\frac{R_n}{R}\,\mathrm{Im}\left[\frac{I_{-1+i\gamma x}(\gamma)I_{1+i\gamma x}(\gamma)}{I^2_{i\gamma x}(\gamma)}\right], \tag{2}$$

$$\beta_I = \frac{R_n}{R}\left(1 - 2\,\mathrm{Re}\left[\frac{\int_0^\gamma I_{i\gamma x}(z)I_{1+i\gamma x}(z)dz}{I^2_{i\gamma x}(\gamma)}\right]\right) - 1. \tag{3}$$

The RSJ model defined by Eq. (1) includes the effect of thermal fluctuations through γ. In the limit where $\gamma \to \infty$, the zero-temperature limit, the RSJ model has a simpler form.[19]

For $I > I_c$, the voltage across the TES is

$$V = R_n[I^2 - I_c(T)^2]^{1/2}, \tag{4}$$

and the resistance in terms of current is

$$R(T,I) = R_n\left[1 - \left(\frac{I_c(T)}{I}\right)^2\right]^{1/2}. \tag{5}$$

The RSJ resistance at finite temperature is bounded by R_n on the high side and by Eq. (4) on the low side. α_I can be calculated by rearranging the partial derivative $\alpha_I = T/(RI)\partial V/\partial T$, and then taking the derivative of Eq. (4) at constant current,

$$\alpha_I = -\frac{R_n^2}{R^2}\frac{I_c(T)}{I^2}T\frac{\partial I_c}{\partial T} = -\frac{R_n^2}{R^2}\frac{I_c(T)^2}{I^2}\frac{\partial \ln I_c}{\partial \ln T}. \tag{6}$$

β_I can be calculated by rearranging the partial derivatives as $\beta_I = 1/(R)\partial V/\partial I - 1$ and taking the derivative of Eq. (4) at constant temperature,

$$\beta_I = \frac{R_n}{R}\frac{1}{\left[1 - \left(\frac{I_c(T)}{I}\right)^2\right]^{1/2}} - 1 = \left(\frac{R_n}{R}\right)^2 - 1. \tag{7}$$

Numerical evaluation of Eqs. (2) and (3) show that, at any given value of I/I_c, Eqs. (6) and (7) give the maximum values of α_I and β_I in the RSJ model.

Now considering the two-fluid model, the voltage across the TES for $I > I_c$ is

$$V = c_R R_n[I - c_I I_c(T)], \tag{8}$$

and the resistance as a function of temperature and current is

$$R(T,I) = c_R R_n\left[1 - c_I\frac{I_c(T)}{I}\right]. \tag{9}$$

In the standard version of the model, $0 \leqslant c_I \leqslant 1$ and $0 \leqslant c_R \leqslant 1$.[15] From Eqs. (1) and (9), the two-fluid resistance is always less than the RSJ resistance for a given I/I_c. The α_I and β_I calculated for the two-fluid model[17] are

$$\alpha_I = -c_I c_R\frac{R_n}{R}\frac{I_c(T)}{I}\frac{\partial \ln I_c}{\partial \ln T}, \tag{10}$$

assuming c_I and c_R are not a function of T, and

$$\beta_I = c_R\frac{R_n}{R} - 1, \tag{11}$$

assuming that I_c and c_R are not a function of current.

In the PSL model, Λ_{Q^*} is assumed to have weak temperature dependence, causing c_R to increase with temperature, eventually reaching a limit of $c_R = 1$ before reaching the normal state. This temperature dependence does not change the expression for β_I [Eq. (11)] but gives additional terms for α_I [Eq. (10)], the consequences of which are not relevant for the model comparison in this Rapid Communication and will be addressed in a future paper.

Also within the PSL model, there are discrete points in the transition where N changes by an integer amount based on the total current in the TES. Over most of the transition, the TES is biased between changes in N. However, near a change in N, c_R could have a nonzero positive derivative with respect to current and Eq. (11) would then have an additional term that increases β_I. Hence β_I is given by Eq. (11) over most of the transition,

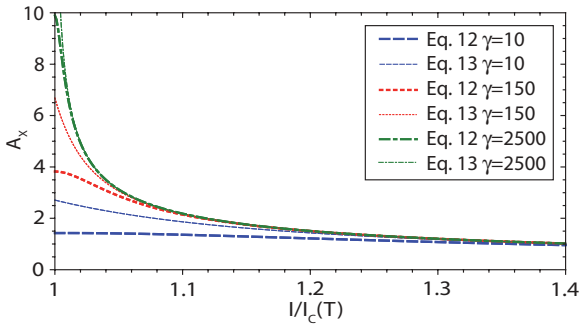

FIG. 2. (Color online) A_x and A_{x0} as a function of I/I_c for various values of γ.

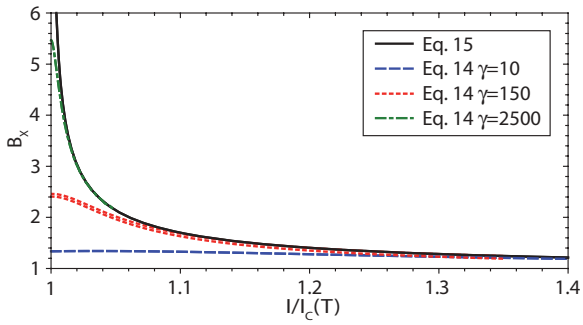

FIG. 3. (Color online) B_x as a function of I/I_c for various values of γ along with B_{x0}.

but increases in the number of PSLs can make higher values of β_I accessible to the two-fluid model in localized regions of the transition.

With $c_R = 1$ and $c_I = 1$, Eqs. (9)–(11) reproduce the expected behavior of an idealized infinitely long superconducting wire. Both the RSJ and two-fluid models have a theoretical basis in their respective regimes, and as L/ξ increases there is a smooth transition from weak-link behavior to two-fluid behavior. The two-fluid model encompasses a range of scenarios, e.g., an idealized infinite superconducting wire for $c_I = 1$ and $c_R = 1$ or PSLs for $c_I < 1$ and $c_R \leqslant 1$. We can now compare the relevant metrics (α_I and β_I) between the two models and establish the maximum and minimum values as a function of I/I_c and γ. We begin by comparing the predictions of the models for α_I but will find that it is most useful to compare predictions of β_I.

Assuming that $c_R = 1$ and $c_I = 1$, α_I for the RSJ and two-fluid models [Eqs. (2) and (10)] differ by a multiplicative factor

$$A_x = \gamma \,\mathrm{Im}\left[\frac{I_{-1+i\gamma x}(\gamma) I_{1+i\gamma x}(\gamma)}{I^2_{i\gamma x}(\gamma)}\right]. \tag{12}$$

When $A_x = 1$ the values α_I are the same for the two models. In Fig. 2, A_x is plotted as a function of I/I_c for several values of γ. At smaller values of I/I_c, the values of A_x are bigger than 1 so that the values α_I in the RSJ model are bigger than in the two-fluid model. The same comparison for the $\gamma \to \infty$ case from Eq. (6) gives

$$A_{x0} = \frac{R_n}{R}\frac{I_c(T)}{I}. \tag{13}$$

A_{x0} is plotted in Fig. 2 for the same values of γ as were plotted for A_x. For larger values of I/I_c, A_{x0} is a good approximation of A_x at all values of γ. The derivative of I_c with respect to T that is in the expressions for α_I in both the RSJ and two-fluid model means that the models cannot be compared to data without assuming a temperature dependence for the critical current or measuring it explicitly.

For β_I, Eqs. (3) and (11) differ in the first term by the multiplicative factor

$$B_x = 1 - 2\,\mathrm{Re}\left[\frac{\int_0^\gamma I_{i\gamma x}(z) I_{1+i\gamma x}(z)dz}{I^2_{i\gamma x}(\gamma)}\right]. \tag{14}$$

In Fig. 3, B_x is plotted as a function of I/I_c for the same values of γ as in Fig. 2. In the regime of interest when $I/I_c > 1$, $B_x \geqslant 0$, and therefore the RSJ model always gives a larger β_I than the two-fluid model for $c_R = 1$. At values of $I/I_c \gg 1$, B_x goes to unity, and we recover the two-fluid model. Also, for small values of γ, B_x is small and almost constant. Returning to $\gamma \to \infty$ in Eq. (7), we define

$$B_{x0} = \frac{1}{\left[1 - \left(\frac{I_c(T)}{I}\right)^2\right]^{1/2}}. \tag{15}$$

B_{x0} is also plotted in Fig. 3 as a black solid line. Any β_I predicted by the RSJ model will be bounded by Eq. (7) on the high side and the two-fluid model with $c_R = 1$ on the low side.

Using Eq. (7) to obtain the maximum β_I in the RSJ model, which depends only on the bias point, we can define the possible ranges of β_I within the RSJ model. At any bias point, Eq. (7) $\geqslant \beta_I$ [Eq. (3)] $\geqslant$ Eq. (11), $c_R = 1$. Assuming $c_R \leqslant 1$, we can also define the range of β_I in the two-fluid model, Eq. (11) ($c_R = 1$) $\geqslant \beta_I$ [Eq. (11), $c_R \leqslant 1$]. Figure 4 shows these expressions plotted as a function of R/R_n, dividing the regions of possible β_I between a region consistent with the RSJ model (upper red shaded region) and a region consistent with the two-fluid model (lower blue shaded region).

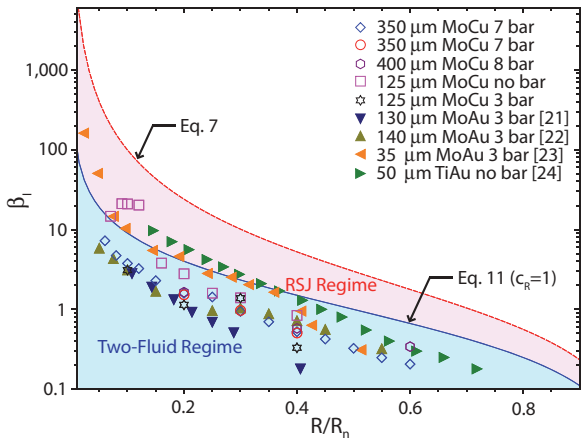

FIG. 4. (Color online) β_I as function of R/R_n for the two-fluid model with $c_R = 1$ (blue solid line) and the zero-temperature RSJ model (red dashed line). The region between the two lines contains the possible values of β_I from Eq. (3), and the values below the blue solid line are the possible values from Eq. (11). The points are measured values of β_I for TESs of various sizes and different bilayer materials as described in the legend.

Figure 4 shows measured values of β_I at various bias values for a number of different devices. The open symbols are for MoCu TESs fabricated at NIST Boulder, while the solid symbols are measured values from the literature. For the devices fabricated and measured at NIST, the values of β_I are extracted from simultaneous fits to the complex impedance at the different bias points. The blue diamonds and red circles are measured β_I values for 350×350 μm^2 x-ray TESs with seven Cu bars for noise mitigation.[20] The TESs corresponding to the red circles were previously analyzed and compared to the two-fluid model.[17] The purple hexagons are for a 400×400 μm^2 TES with eight Cu bars, optimized for gamma-ray spectroscopy.[10] Finally the magenta squares and black stars are for a 125×125 μm^2 TESs with no Cu bars and three Cu bars, respectively.

Also shown in Fig. 4 are recently published values of β_I from other groups measuring TESs of different sizes and using different materials. The blue downward-pointing, dark yellow upward-pointing, and orange left-pointing triangles are from 130×130 μm^2,[21] 140×140 μm^2,[22] and 35×35 μm^2 (Ref. 23) MoAu TESs, respectively, all with three Au bars. Finally the green right-pointing triangles are from a 50×50 μm^2 TiAu TES with no bars.[24]

The measured β_I in Fig. 4 represent a broad range of TESs. However, the majority of the measured values are in a range of β_I that is not accessible within the RSJ model. Only the smallest devices (<125 μm) at low bias ($<30\%$ R_n) values have β_I in the RSJ regime. It is logical that smaller TES films where $L < \xi$ have stronger RSJ behavior. Some of the MoAu TESs in Fig. 4 have superconducting electrodes with an elevated T_c due to an additional Nb layer[23] that may extend the order parameter further into the TES. Except in the 35 μm device, the β_I of TESs with normal-metal bars are in the two-fluid regime across the whole transition. This is consistent with an increase in the effective length of the TES as the current meanders around the bars low in the transition.[25] This is also supported by the 3-bar 125 μm MoCu device having lower β_I values at 10% and 20% R_n than the no-bar device that is the same size. In the larger TES devices, at typical bias points with $R > 10\%$ R_n, there is not enough wave function overlap for the leads to do much more than reduce the effective length of the TES. In this regime, the two-fluid model is more appropriate.

Although the smaller devices show a higher β_I for $R/R_n \ll 1$, they quickly converge with the larger devices as the bias is increased. This could be explained by the TES going from a superconducting state toward a normal state, causing the weak link to transition from a SS′S structure to a SN′S structure [Fig. 1(b)]. In a SN′S weak link with an L just a few times greater than ξ, the supercurrent through the weak link drops exponentially with increased L.[13] However, in a SS′S weak link the order parameter decreases to a nonzero constant value that is dependent on the properties of the S′ material, and the weak-link behavior can occur at much greater lengths. The I_c for long SS′S weak links can also be much higher than for the same-sized SN′S weak link.[26] This implies that the physics describing the transition of the TES film from the superconducting state to the normal state is critical to understanding the temperature- and current-dependent TES resistance. It also suggests that only in very small devices, where the weak-link behavior is maintained in the finite resistance regime, will the TES resistance be dominated by its weak-link behavior.[12]

An important factor limiting the development of models that describe the temperature- and current-dependent resistance of a TES is a lack of direct comparisons to measured devices at realistic operating conditions. This unfortunate deficit is likely due to a lack of expressions for the important TES parameters α_I and β_I. We have derived simple expressions for the upper and lower limits of α_I and β_I within the RSJ model as proposed by Kozorezov *et al.*[14] and illustrated how these relate to the same parameters in the two-fluid model.[17] These simple expressions allow direct comparison of these models as a function of R/R_n to the available data.

The expressions for β_I are especially straightforward and suggest that most TES devices are more reasonably described by the two-fluid model. The smallest devices show evidence of weak-link behavior at low biases but quickly converge to the predictions of the two-fluid model as the TES becomes more resistive. Similarly simple expressions were derived for α_I and could be compared to data if measurements of $I_c(T)$ at the relevant temperatures were available. Together, these measurements across a broad array of TES devices should help produce a better understanding of the resistive transition that is at the foundation of these successful detectors.

The authors acknowledge the support of the US Department of Energy through the Office of Nonproliferation Research and Development.

*Also at University of Denver, Denver, CO 80208, USA; Douglas.Bennett@nist.gov

†Also at University of Colorado, Boulder, CO 80309, USA.

[1] S. Das, T. A. Marriage, P. A. R. Ade *et al.*, Astrophys. J. **729**, 62 (2011).

[2] S. Das, B. D. Sherwin, P. Aguirre *et al.*, Phys. Rev. Lett. **107**, 021301 (2011).

[3] A. van Engelen, R. Keisler, O. Zahn *et al.*, Astrophys. J. **756**, 142 (2012).

[4] B. D. Sherwin, J. Dunkley, S. Das *et al.*, Phys. Rev. Lett. **107**, 021302 (2011).

[5] C. L. Reichardt, R. de Putter, O. Zahn, and Z. Hou, Astrophys. J. Lett. **749**, L9 (2012).

[6] N. Hand *et al.*, Phys. Rev. Lett. **109**, 041101 (2012).

[7] K. Irwin and G. Hilton, in *Cryogenic Particle Detection*, Topics In Applied Physics, Vol. 99 (Springer, Berlin, 2005), pp. 63–149.

[8] D. B. Thorn, M. F. Gu, G. V. Brown, P. Beiersdorfer, F. S. Porter, C. A. Kilbourne, and R. L. Kelley, Phys. Rev. Lett. **103**, 163001 (2009).

[9] J. Ullom, J. Low Temp. Phys. **151**, 746 (2008).

[10] A. Hoover, N. Hoteling, M. Rabin, J. Ullom, D. Bennett, P. Karpius, D. Vo, W. Doriese, G. Hilton, R. Horansky, K. Irwin, V. Kotsubo, D. Lee, and L. Vale, Nucl. Instrum. Methods A **652**, 302 (2011).

[11] The CDMS II Collaboration, Science **327**, 1619 (2010).

[12] J. E. Sadleir, S. J. Smith, S. R. Bandler, J. A. Chervenak, and J. R. Clem, Phys. Rev. Lett. **104**, 047003 (2010).

[13] K. Likharev, Rev. Mod. Phys. **51**, 101 (1979).
[14] A. Kozorezov, A. A. Golubov, D. D. E. Martin, P. A. J. de Korte, M. A. Lindeman, R. A. Hijmering, J. van der Kuur, H. F. C. Hoevers, L. Gottardi, M. Y. Kupriyanov, and J. K. Wigmore, Appl. Phys. Lett. **99**, 063503 (2011).
[15] K. D. Irwin, G. C. Hilton, D. A. Wollman, and J. M. Martinis, J. Appl. Phys. **83**, 3978 (1998).
[16] W. Skocpol, M. Beasley, and M. Tinkham, J. Low Temp. Phys. **16**, 145 (1974).
[17] D. Bennett, D. Swetz, R. Horansky, D. Schmidt, and J. Ullom, J. Low Temp. Phys. **167**, 102 (2012).
[18] W. T. Coffey, Y. P. Kalmykov, S. V. Titov, and L. Cleary, Phys. Rev. E **78**, 031114 (2008).
[19] V. Ambegaokar and B. Halperin, Phys. Rev. Lett. **22**, 1364 (1969).
[20] J. N. Ullom, J. A. Beall, W. B. Doriese, W. D. Duncan, L. Ferreira, G. C. Hilton, K. D. Irwin, C. D. Reintsema, and L. R. Vale, Appl. Phys. Lett. **87**, 194103 (2005).
[21] N. Iyomoto, S. R. Bandler, R. P. Brekosky, A.-D. Brown, J. A. Chervenak, F. M. Finkbeiner, R. L. Kelley, C. A. Kilbourne, F. S. Porter, J. E. Sadleir, S. J. Smith, and E. Figueroa-Feliciano, Appl. Phys. Lett. **92**, 013508 (2008).
[22] S. Smith, S. Bandler, A.-D. Brown, J. Chervenak, E. Figueroa-Feliciano, F. Finkbeiner, N. Iyomoto, R. Kelley, C. Kilbourne, F. Porter, and J. Sadleir, J. Low Temp. Phys. **151**, 195 (2008).
[23] S. Smith, J. Adams, C. Bailey, S. Bandler, J. Chervenak, M. Eckart, F. Finkbeiner, R. Kelley, C. Kilbourne, F. Porter, and J. Sadleir, J. Low Temp. Phys. **167**, 168 (2012).
[24] M. Lindeman, P. Khosropanah, R. A. Hijmering, M. Ridder, L. Gottardi, M. Bruijn, J. van der Kuur, P. A. J. de Korte, J. R. Gao, and H. Hoevers, J. Low Temp. Phys. **167**, 96 (2012).
[25] D. S. Swetz, D. A. Bennett, K. D. Irwin, D. R. Schmidt, and J. N. Ullom, Appl. Phys. Lett. **101**, 242603 (2012).
[26] H. J. Fink and R. S. Poulsen, Phys. Rev. B **19**, 5716 (1979).